

Main Manuscript for

Quantifying electron transport in aggregated colloidal suspensions in the strong flow regime

Julie B. Hipp^{b,c,1}, Paolo Z. Ramos^{a,1}, Qingsong Liu^a, Norman J. Wagner^b, Jeffrey J. Richards^{a,*}

^a Department of Chemical and Biological Engineering, Northwestern University, Evanston, IL 60208, USA

^b Center for Neutron Science, Department of Chemical and Biomolecular Engineering, University of Delaware, Newark, DE 19716, USA

^c Current affiliation: Julie B. Hipp, The Procter & Gamble Company, Cincinnati, OH 45202, USA

* Corresponding author: Jeffrey J. Richards

Email: jeffrey.richards@northwestern.edu

Author Contributions: N.J.W. and J.J.R. designed research; J.B.H. and P.Z.R. performed research; J.B.H., P.Z.R., Q.L., and J.J.R. analyzed data and wrote the paper.

Competing Interest Statement: The authors declare the following financial interests/personal relationships which may be considered as potential competing interests: Jeffrey John Richards reports financial support was provided by National Science Foundation.

Classification: Physical Sciences, Applied Physical Sciences

Keywords: Carbon Black, Rheology, Electrical Conductivity, Electron Transport

This PDF file includes:

Main Text Figures 1 to 4

Abstract

Electron transport in complex fluids, biology, and soft matter is a valuable characteristic in processes ranging from redox reactions to electrochemical energy storage. These processes often employ conductor-insulator composites in which electron transport properties are fundamentally linked to the microstructure and dynamics of the conductive phase. While microstructure and dynamics are well-recognized as key determinants of the electrical properties, a unified description of their effect has yet to be determined, especially under flowing conditions. In this work, the conductivity and shear viscosity are measured for conductive colloidal suspensions to build a unified description by exploiting both recent quantification of the effect of flow-induced dynamics on electron transport and well-established relationships between electrical properties, microstructure, and flow. These model suspensions consist of conductive carbon black particles dispersed in fluids of varying viscosities and dielectric constants. In a stable, well-characterized shear rate regime where all suspensions undergo self-similar agglomerate breakup, competing relationships between conductivity and shear rate were observed. To account for the role of variable agglomerate size, equivalent microstructural states were identified using a dimensionless fluid Mason number, Mn_f , which allowed for isolation of the role of dynamics on the flow-induced electron transport rate. At equivalent microstructural states, shear-enhanced particle-particle collisions are found to dominate the electron transport rate. This work rationalizes seemingly contradictory experimental observations in literature concerning the shear-dependent electrical properties of carbon black suspensions and can be extended to other flowing composite systems.

Significance Statement

Electrically driven processes such as electrochemistry for energy storage devices and electrosorption for water desalination electrodes require the efficient transport of electrons by conductive additives incorporated into a non-conductive fluid matrix. Transport in these systems depends on the processing-dependent microstructure, but the mechanism remains unidentified. This work establishes a relationship between the flow-dependent microstructure and electron hopping rate by leveraging rheo-electric measurements of well-studied model conductive carbon black suspensions. The flow-dependent electrical properties are analyzed considering recent identification of how flow-induced dynamics play a role in determining the rate of electron transport. We anticipate these findings will have an impact in the definition of formulation and processing windows for applications including emerging electrochemical energy storage methods and water deionization technologies.

Main Text

Introduction

Electron transport is a fundamental attribute found in natural processes, such as photosynthesis and respiration, and engineered technologies including tires, batteries, and water deionization (1-3). Many of these systems utilize composites consisting of conductive fillers in an electrically insulating matrix. The use of these composites introduces flexibility by leveraging the properties of the individual components but also adds complexity, such as a nontrivial dependence of the electrical conductivity on the dispersion quality of the conductive filler phase (4-7). Of particular interest are suspensions of conductive particles in an electrically insulating fluid that demonstrate an intimate connection between electron transport and applied shear (8-10). Motivated to engineer a desired conductivity in these suspensions with low viscosities (11, 12), researchers have analogized their electrical behavior to that of static polymer composites (13, 14). tying electron transport to the microstructure. While this assumption, combined with flowmicrostructure and flow-property relationships, can be used to build connections between flowinduced microstructural evolution and the electrical conductivity, a comprehensive picture has vet to emerge (15–17). A missing piece to fully understand the electron transport in these systems is the contribution from flow-induced particle dynamics, which was recently identified as a function of particle-particle collisions for non-Brownian suspensions (18). This presents a unique opportunity to establish the fundamental origins of electron transport in suspensions of conducting particles by evaluating the role that dynamics plays in model, well-studied conductive colloidal slurries under

Due to widespread use as a conductive additive, carbon black (CB) incorporated in various continuous phases is a model system used to understand the relationship between microstructure, flow behavior, and electrical conductivity. When suspended in a fluid, CB primary aggregates form micron-scale agglomerates due to van der Waals attractions. These agglomerates grow both in size and number density with increasing concentration and eventually jam and bond with one another to form a physical, system-spanning, stress-bearing network (19, 20). The link between electron transport rate and quiescent or static CB microstructure is well-established as a nonlinear function of agglomerate volume fraction (15, 21–25). However, electron transport for CB-filled suspensions does not require a network of inter-agglomerate bonds and is instead mediated by electron tunneling or hopping in which electrons travel over finite inter-agglomerate gaps (13, 26). This structure-property relationship is complemented by many rheological studies focused on understanding the shear-dependent rheology and microstructure of CB-filled systems.

Under flow, the CB network yields and agglomerates transiently reorganize to a new steady-state structure (27). Changes in viscosity, yield stress, or elastic modulus are often attributed to changes in agglomerate microstructure (22, 28–30). Direct measurements of the shear-induced CB microstructure were performed using rheo-optical methods by Osuji and Weitz, who identified three structural regimes and their rheological indicators (31, 32). In an extension of this landmark work, simultaneous rheological and neutron scattering measurements were used to quantify the shear-dependent agglomerate structure as well as the transition between these regimes (33, 34). This combination of work concludes that a stable, predictable flow behavior can be measured under high shear intensities where the instantaneous stress response of the suspension is well above the network yield stress. Subjected to strong flow, CB agglomerates undergo a self-similar change in size that depends on the relative magnitudes of the density and strength of inter-agglomerate bonds and the strength of the flow (33, 34).

Although such well-established relationships between flow and microstructure explain the rheological behavior of CB suspensions, they fail to reconcile contradicting trends in reported shear-dependent electrical conductivity (1, 21, 23, 25, 35, 36). For example, suspensions of CB in various Newtonian fluids exhibit either an increase (1, 23, 35) or a decrease (21, 25, 36) in electrical conductivity with increasing shear rate. Notably, CB suspended in high dielectric constant fluids exhibits a shear-enhancement in conductivity while the opposite behavior is observed for suspensions prepared in low dielectric constant fluids. To reconcile these opposing trends, two competing effects of either microstructural or dynamical origins have been proposed: a decrease in conductivity due to break-up of agglomerates (25) and an increase due to higher frequency of

particle-particle collisions (21). However, no unified explanation or quantitative relationship between flow and electron transport in these suspensions have been established.

To build such quantitative relationships and further understand the fundamental origins of electron transport in flowing CB suspensions, we measured and analyzed the shear-dependent electrical properties of CB suspended in fluids of various viscosities and dielectric constants. To account for shear-induced changes in the microstructure, the conductivity and rate of electron transport were measured in the strong flow regime, where the agglomerates undergo self-similar break up with increasing shear intensity. In this shear rate regime, similar shear-dependent microstructural states were identified across all suspensions, allowing for direct analysis of the effect of dynamics on the electrical properties. The flow-induced dynamical contribution to the electron transport behavior was then further isolated by comparing measurements performed in the quiescent and sheared states. Finally, this flow-dependent dynamic conductivity is understood in terms of existing frameworks based on the electrical diffusivity of non-Brownian suspensions by accounting for the volume fraction-dependent rate of flow-induced collisions. This combination of experiments and analysis provide a unified understanding of the role that shear-induced changes in microstructure and dynamics play in determining electron transport in CB suspensions that has broader application to composite systems and their technological applications more generally.

Results and Discussion

Viscosity Behavior in Strong Flow

Using methodology developed in previous work (29, 33), the strong flow regime was identified for suspensions of a model, conductive CB formulated in four suspending fluids with broad variation in both viscosity and dielectric constant (Table S1). As an example of the measured rheological behavior, the stress, σ , and viscosity, η , measured at 0 and 3 minutes are plotted against the applied shear rate, $\dot{\gamma}$, for the effective volume fraction ϕ_{eff} = 0.12 CB suspension in hexadecane in Figure 1a. The strong flow regime is highlighted in grey and exhibits shear-thinning regardless of the duration of shear. At lower shear rates, a transient response is evident where the stress at 3 minutes exhibits rheopexy, a drop of σ and η with time upon step down in shear rate. Prior work has established this rheopexy to originate from the heterogeneity and densification of agglomerates that develop in the weak flow regime. For the presented sample specifically, this regime resides below a transitional shear rate of ~500 s⁻¹, defined quantitatively by comparing the stress response at an applied shear rate to the apparent yield stress, σ_v , from the instantaneous flow curve (33). Rheological measurements on all suspensions show that this shear-thinning behavior is common for all 12 suspensions tested, with variability in the transitional shear rate that depends on the effective volume fraction and the identity of the suspending fluid (Figure S1). The relative viscosity, $\eta_r = \eta/\eta_f$ where η is the measured suspension viscosity and η_f is the suspending fluid viscosity, for all suspensions of hexadecane (HD), mineral oil (MO), propylene carbonate (PC) and ethylene glycol (EG) versus the applied shear rates in the strong flow regime is plotted in Figure 1b. The shear-dependent viscosity is characterized by a power law that scales with an exponent between -0.4 and -0.9. Larger values correspond to higher suspending fluid viscosities and larger effective volume fractions. Furthermore, η_r increases with the effective volume fraction for suspensions in the same solvent and decreases at the same volume fraction for suspensions with lower suspending fluid viscosity.

Defining an Equivalent Microstructural Basis

Previous measurements of the shear-dependent microstructure show that the CB agglomerate size is larger when the viscosity of the solvent is lower (34). This relationship can be rationalized by the fluid Mason number, Mn_f , which is the dimensionless balance of the shear forces applied by the continuous phaseand the cohesive forces tying agglomerates together, defined as

$$Mn_f = \frac{6\pi\phi_{eff}^2\eta_f\dot{\gamma}}{\sigma_y} = \frac{fluid\ shear\ forces}{cohesive\ forces}$$
[1]

where ϕ_{eff} is the effective primary aggregate volume fraction, η_f is the suspending fluid viscosity, $\dot{\gamma}$ is the applied shear rate, and σ_y is the apparent yield stress, as previously described. Here, σ_y was obtained from a fit of the Herschel-Bulkley model (37, 38) to the instantaneous flow curve (33) (**Figure S2**). Although the entirety of the underlying physics governing shear-induced agglomerate breakup is not included in the fluid Mason number, this dimensionless group enables a qualitative assessment of the relative extent of agglomerate breakup with increasing shear intensity at a given effective volume fraction (39).

To illustrate the common structure-property relationship underlying these flow curves across the various suspension compositions, the relative viscosities are plotted versus Mn_f for shear rates identified in the strong flow regime. As seen in the top panel of **Figure 1c**, this representation creates a master curve across all solvent types for a given effective volume fraction. This observation is consistent with a similar collapse of η_r versus Mn_f for CB suspensions prepared in solutions of n-methyl pyrrolidone and polyvinyl difluoride (15). The difference in master curves for different effective volume fractions is due to the difference in the number density of agglomerates at the same values of Mn_f . Thus, Mn_f proves to be a valuable predictor of the rheological state, accounting for the differences in solvent properties and correctly describing the variation in η_r with volume fraction and suspending fluid viscosity.

To compare with prior measurements, the hydrodynamic agglomerate volume fraction, ϕ_{aaal} , was estimated by rearranging the Krieger-Dougherty equation such that (40)

$$\phi_{aggl} = \phi_m \left(1 - \eta_r^{-\frac{1}{2.5\phi_m}} \right)$$
 [2]

with ϕ_m as the maximum packing fraction of 0.64. Building upon ϕ_{eff} , which accounts for the porosity of primary aggregates, ϕ_{aggl} describes the relative volume occupied by carbon black agglomerates by accounting for the immobile fluid trapped within the agglomerate structure in addition to the solid carbon black particles. Subsequently, the agglomerate size, $R_{g,aggl}$, relative to the primary aggregate size, a, was determined as (41)

$$R_{g,aggl}/a = \left(\phi_{aggl}/\phi_{eff}\right)^{\frac{1}{3-d_f}}$$
 [3] assuming a constant fractal dimension, d_f , of 2.5 based on previous scattering measurements (34,

assuming a constant fractal dimension, d_f , of 2.5 based on previous scattering measurements (34, 39). The bottom panel of **Figure 1c** shows master curves of $R_{g,aggl}/a$ that decreases with Mn_f as higher shear forces act to break up the CB microstructure. This effect becomes less prominent as ϕ_{eff} increases due to the denser packing and overall smaller size of the agglomerates. This analysis agrees with previous results from direct structural measurements via scattering of the shear-dependent agglomerate size (34). While the calculation of $R_{g,aggl}/a$ stems directly from η_r , this representation confirms that Mn_f sets an equivalent microstructural basis for comparison of the electrical properties across all suspending fluids at a fixed CB loading.

Analysis of the Frequency-dependent Conductivity

Impedance spectroscopy measurements were obtained simultaneously with the rheological measurements under steady flow at shear rates in the strong flow regime. The conductivity spectra, κ , as a function of frequency, ω , of unsheared ϕ_{eff} = 0.12 CB in HD and PC are shown in **Figure 2a**. Two distinctive features can be observed in both samples: an alternating current (AC) upturn at high frequencies and a direct current (DC) asymptote regime at lower frequencies. In an ideal semiconducting material, the low frequency regime plateaus to a constant DC conductivity such that $\kappa_{DC} = \kappa(\omega \to 0)$ (42). While this relationship is observed in the non-polar suspending fluids of MO and HD, it is not observed in the polar suspending fluids of PC and EG (**Figure S3**). Instead, the conductivity decreases further with decreasing frequency. This phenomenon is well-understood as electrode polarization (19), where ions dissolved in the polar fluids accumulate at the electrode and CB surfaces and develop a non-uniform electric field.

The transition between the AC upturn and the DC asymptote divides the high-frequency polarization of a conductive cluster from the delocalization of electrons responsible for the pseudo-DC behavior (42). The characteristic frequency that marks the convergence of the features then describes the time-scale of electron transport through the suspension. To extract this frequency,

the AC upturn was fit to a power law dependence given as $\kappa = A\omega^s$, where A is a constant and s is the characteristic exponent of the AC conductivity. Similarly, the DC asymptote prior to the effects of electrode polarization was fit to the same power law dependence to isolate the electrical response from the ionic effects. These fits intersect at the characteristic frequency, ω_c that defines the electron transport time, τ . Instead of reporting the conductivity at an arbitrary frequency in the DC asymptote, we report the conductivity at ω_c from the power law conjunction, referred to as the characteristic conductivity, κ_c . In doing so, we avoid the effects of electrode polarization while remaining in the high frequency limit of the DC conductivity. This model-independent framework was used to obtain these parameters for all samples at rest and sheared in the strong flow regime regardless of the polarity of the suspending fluid. Note that the data quality of the ϕ_{eff} = 0.27 PC suspension was insufficient to determine τ with certainty and is subsequently excluded (**Figure S4**).

Dielectric Trends in Strong Flow

As shown in **Figure 2b-c**, interesting trends emerge in both τ and κ_c as functions of CB loading, suspending fluid properties, and applied shear rate. All suspensions exhibit a step increase in τ when sheared from the quiescent state, indicating a fundamental change in the dominant pathway for electron transport. In the quiescent state, the system-spanning inter-agglomerate bonds are continuous and provide a pathway for electron transport. Under flow, these interagglomerate bonds are broken and electrons must hop across finite inter-agglomerate gaps. In the latter case, electron transport is constrained by the distance of the inter-agglomerate gap and the number of gaps to overcome. This in turn relates to the agglomerate microstructure that has been shown to depend on the suspending fluid properties and the applied shear rate. The dependence on these factors can be observed in **Figure 2b**, where τ increases as a function of $\dot{\gamma}$ due to an increase in size and number of inter-agglomerate gaps as the agglomerate size decreases. The weakening dependence of au on $\dot{\gamma}$ with increasing ϕ_{eff} suggests a concurrent enhancement of electron transport time that occurs with increasing $\dot{\gamma}$. This indicates a complex relationship between electron transport time, shear-dependent agglomerate size, and agglomerate dynamics. κ_c shows a different, similarly complex dependence on the shear rate even though the microstructural and rheological behaviors are the same in the strong flow regime. For the PC suspensions, κ_c steadily increases above the quiescent state value with $\dot{\gamma}$. The opposite trend is observed for MO and HD where instead κ_c decreases from the quiescent state value with $\dot{\gamma}$ across all effective volume fractions. Surprisingly, a combination of behaviors is seen for suspensions in EG, where κ_c decreases with $\dot{\gamma}$ for the lowest effective volume fraction but increases with $\dot{\gamma}$ at higher effective volume fractions.

In addition to these shear-dependent trends, as ϕ_{eff} increases, a decrease in au and an increase in κ_c are observed across all suspensions. The volume fraction dependence is consistent with both an increase in the bulk conductivity and electron transport rate as additional CB particles decrease the inter-agglomerate distance and increase the number of conductive pathways through the fluid (23, 25, 36). When comparing across solvents, the dielectric constant of the suspending fluid, ε_f , displays a significant role in the relative magnitude of κ_c . PC ($\varepsilon_f = 64$) and EG ($\varepsilon_f = 37$) have significantly higher κ_c than HD ($\varepsilon_f = 2$) and MO ($\varepsilon_f = 2$). This is consistent with our understanding of electron transport in these systems where the hopping probability depends on the relative polarizability of the continuous phase (43-45). The dielectric constant cannot explain all trends in κ_c , however, as suspensions formed with HD are universally more conductive than those prepared in MO. This difference in κ_c , between the two nonpolar solvents shows an inverse relationship with viscosity, as MO ($\eta_f = 26 \text{ mPa} \cdot \text{s}$) is more viscous than HD ($\eta_f = 3 \text{ mPa} \cdot \text{s}$). This dependence on viscosity can be attributed to the effect of shear stress on the average agglomerate size, as depicted in Figure 1c, where higher stresses lead to smaller agglomerates and therefore, lower conductivities due to limitations by inter-agglomerate transport (21, 25). In addition, suspensions formed in EG show higher conductivity than suspensions in PC. We attribute this to the protic nature of the solvents, where it has been shown that protic solvents facilitate electron tunneling relative to aprotic solvents (44). This further demonstrates the convoluted response of κ_c with the suspending fluid properties.

In a similar fashion, τ rises with increasing η_f , further suggesting that smaller agglomerates lead to slower electron transport rates. Aside from this trend, the dependence of τ on the suspending fluid properties does not follow the same behavior of κ_c . For example, suspensions in polar liquids in general have smaller magnitudes of τ than those in nonpolar liquids, indicating that the inter-agglomerate electron transport rate is directly related to ε_m . Prior work has shown that τ and κ_c are linked through the dielectric strength $\Delta\varepsilon$ via the relation $\kappa_c = p\varepsilon_0\Delta\varepsilon/\tau$, where p is a phenomenological constant and ε_0 is the permittivity of free space (46). While our frequency-dependent dielectric data is not sufficiently broadband to estimate $\Delta\varepsilon$ in all cases, we are able to identify the static permittivity, ε_s , by identifying the plateau in the real component of the complex permittivity. A comparison of κ_c versus $\varepsilon_0\Delta\varepsilon/\tau$ shows a strong correlation with a prefactor p determined by the polarity of the solvent (46) (**Figure S5**). This confirms that the high frequency polarization responsible for the upturn in the AC conductivity is influenced by the low-frequency DC conduction. These observations of τ and κ_c demonstrate that electron transport in CB suspensions cannot be understood by only considering the suspending fluid properties and further points to the nontrivial role of the changing microstructure due to the applied shear.

Independent Scaling of Networks

A commonly held view for quiescent CB gels is that physical connections within the agglomerate network is not the primary pathway available for electron transport (14, 19). A previous study of CB suspended in MO showed that the same conductivity can be achieved in gels with different elasticity, indicating discrete networks of stress-bearing bonds and percolated electrical pathways (25). To probe the relationship between the elasticity and quiescent conductivity, we performed small amplitude oscillatory shear experiments on all suspensions after flow cessation from $\dot{\gamma} = 2500 \text{ s}^{-1}$ (Figure S6). All suspensions exhibit a gel-like response with a frequency independent storage modulus that far exceeds the loss modulus, commonly observed for viscoelastic materials with a yield stress (20, 47). The plateau modulus, G_0 , was determined by averaging the storage modulus across the probed frequency domain from Figure S6 and plotted against the quiescent characteristic conductivity, $\kappa_{c,\gamma=0}$, from **Figure 2C** in **Figure 3a**. As expected, as the effective volume fraction increases, G_0 and $\kappa_{c,\gamma \doteq 0}$ rises, which can be attributed to an increase in the number of mechanical contacts and decrease in interagglomerate distances (20). Despite similar network architectures and elasticities at equivalent effective volume fractions, however, CB suspended in polar solvents display higher conductivites than that of nonpolar solvents by a factor of 100. These differences follow the dependence of electron transport on the dielectric nature of the fluid. In general, higher conductivities are achieved when moving from nonpolar to polar aprotic and finally to polar protic solvents (43-45). These results provide evidence for two independent network pathways: one that determines the electrical conductivity and one that determines the elasticity.

Comparison to a Static Conductivity Model

An observation from **Figure 2c** is that upon shearing, κ_c remains finite after the system-spanning agglomerate microstructure yields and continues to evolve. To compare the sheared and quiescent case, we normalize the characteristic conductivity of the suspensions under flow to the quiescent value such that $\hat{\kappa} = \kappa_c/\kappa_{c,\gamma=0}$ and plot it against the agglomerate volume fraction, ϕ_{agg} , derived from Equation 4. As these suspensions undergo reversible, self-similar microstructural evolution with decreasing shear rate (33), one would expect the conductivity at rest to be identical to the conductivity in flow approaching maximum packing. However, **Figure 3b** shows that $\hat{\kappa}$ does not approach 1 in the limit of $\phi_{aggl} \rightarrow 0.64$ for the $\phi_{eff} = 0.12$ CB samples. As the quiescent conductivities after flow cessation do not vary significantly with each step down in shear rate, we believe that this trend in $\hat{\kappa}$ is not due to changes in the anisotropy of the arrested CB network or sedimentation (**Figure S7**). This leads to the hypothesis that the electrical properties and mechanism of electron transport under flow are distinct from those in the quiescent state regardless of the solvent choice.

The electrical conductivity of nanocomposites is often assumed to originate from electrons hopping between conductive carbon fillers in a non-conductive matrix. One prevalent framework is the critical path model (13) that describes an enhancement in the conductivity with smaller filler sizes, higher volume fractions, and shorter average separation distances. As shear flow changes $R_{g,aggl}/a$ and ϕ_{aggl} , it is possible to directly compare the results in **Figure 3b** with the predicted conductivity from the critical path model. Several estimates of the conductivity normalized to that at $\phi_{aggl} = 0.64$ are shown by the dashed curves for a series of dimensionless hopping distances, $\hat{\xi} = \xi/a$. For our range of parameters, the predicted normalized conductivity is more dependent on ϕ_{aggl} than $R_{g,aggl}/a$. It is particularly sensitive at a $\hat{\xi}$ value of 0.01 that is within the hopping distance length scale predicted by Ambrosetti et al. for spherical carbon nanoparticles (13, 48, 49). While the shapes of the curves qualitatively share some features with the nonpolar CB suspensions, the model fails to capture the normalized conductivites of the polar CB suspensions, which remarkably increase as ϕ_{aggl} decreases. Additionally, the model cannot predict the discontinuity in the conductivity from the quiescent state to that under flow near maximum packing, even for the higher ϕ_{eff} suspensions (**Figure S8**). Combining these two key factors suggests that some relevant dependence on the CB microstructure, solvent, or flow is missing.

Consideration for Particle Interactions

One consequence of translating the critical path model directly to flowing suspensions is the exclusion of the particle dynamics that are not present in static nanocomposites. The role of shear-induced dynamics has recently been isolated for non-Brownian suspensions of conducting spheres at concentrations where no critical path exists for electron transport in the quiescent state (18). For these non-Brownian particles, the conductivity is only finite under shear and is proportional to the electron diffusivity between particles given as a^2/τ where a is the characteristic particle size. For CB suspensions, however, τ remains finite in the absence of shear as electron transport is still permitted through the continuous agglomerate network. In this state, τ represents the fast intraagglomerate transport time, au_{intra} , across carbon-carbon bonds and small hopping distances. Under flow, however, τ becomes a convolution of τ_{intra} and the slower inter-agglomerate transport time, au_{inter} , that arises due to larger gaps that form between particles. To isolate au_{inter} , the shearindependent contribution, au_{intra} , measured in the quiescent state was removed from au obtained at each shear rate such that $\Delta \tau = \tau_{inter} = \tau - \tau_{intra}$. Consequently, the particle diffusivity increases with applied shear rate and particle loading according to a modified collision rate, $a^2\phi\dot{\gamma}g(\phi)$, where $q(\phi)$ is the inverse of the zero-wavevector hard sphere structure factor and describes the enhanced likelihood of interactions at finite volume fraction. For the non-Brownian suspensions, it was found that the time scale for electron diffusivity collapses with this modified collision rate, showing a dependence of the conductivity on particle interactions. The use of this analysis to describe the frequency of shear-induced collisions can be reapplied to the CB suspensions studied here as the strong flow regime corresponds to a Peclet number exceeding 100 for all cases, indicating Brownian diffusion is negligible when describing the particle dynamics. Following this approach, we combined the the particle and electron diffusivity expressions to include contributions of agglomerate collisions to the electron transport time to yield:

$$g(\phi_{eff}) = 1/\phi_{eff}\dot{\gamma}\Delta\tau$$
 [4]

 $g(\phi_{eff}) = 1/\phi_{eff}\dot{\gamma}\Delta\tau \tag{4}$ The calculated values of $g(\phi_{eff})$ were plotted against Mn_f and shown in **Figure 4a**. $g(\phi_{eff})$ decreases with increasing Mn_f across all suspensions, suggesting that agglomerateagglomerate collisions are less probable as the agglomerate size and volume fraction decreases. At the same Mn_f , $g(\phi_{eff})$ shows a weak dependence with ϕ_{eff} and is seemingly more sensitive to the identity of the suspending fluid. Albeit for PC suspensions, values of $g(\phi_{eff})$ for a given solvent almost entirely collapse on top of each other, which cannot be explained with this framework. While the exact nature of the solvent contribution to $g(\phi_{eff})$ is unknown, the change in solvent can be accounted for by rescaling the data sets with an empirical shift factor, α . We chose to rescale all suspensions against the $\phi_{eff}=0.12$ CB suspension in MO as it represents the slowest electron transport rate when under flow. Using this empricial shift factor of order unity, all the data lie on one master curve when plotted against Mn_f with a fit to a power law scaling with - 1.6, as shown in **Figure 4b**. The tight correlation and quantitative agreement of $g(\phi_{eff})$ with Mn_f presents strong evidence that hydrodynamics modify the electron transport rate. Therefore, the electrical diffusivity can theoretically be tuned by shifting the magnitude and expected range of Mn_f for a given CB suspension.

Inspection of the results presented in **Figure 4c** reveals that the variation of the empirical shift factor α with respect to ϕ_{eff} for all suspensions is a factor of order 1. In addition, α decreases with ϕ_{eff} for CB suspensions in MO, HD, and EG while α increases in PC. As previously discussed, α acts to modify $g(\phi_{eff})$ for the difference in the solvent types, whereas the original $g(\phi)$ corresponds to that of hard spheres. Following this line of reasoning, we approximate α using the $g(\phi)^{-1}$ function derived from the Carnahan-Starling approximation used in dense hard-sphere suspensions (50, 51). The decline in predicted values of α with increasing ϕ_{eff} aligns remarkably well with the responses observed in MO and HD, albeit with a constant offset required for quantitative agreement. Increasing the solvent dielectric constant to that of EG deviates from the prediction in that the decrease in α with ϕ_{eff} becomes less prominent, until finally at PC where the response no longer agrees with the Carnahan-Starling expression.

These observations in α imply that predicting the electron transport rate for model CB suspensions requires accounting for the agglomerate hydrodynamics and formulation chemistry. Both aspects would alter the zero-wavevector structure factor and deviate the specific pair potential from hard-sphere behavior. Additional consideration must thus be taken when modifying the suspending fluid properties with surfactants, electrolytes, and active materials that would further augment the interaction between agglomerates. Nevertheless, our empirical collapse of $g(\phi_{eff})$ with Mn_f provide value in formulating suspensions and designing processes for applications where predictable and controllable electron transport rates are required. How our findings map to other carbonaceous additives, such as carbon nanotubes and graphene, as well as broader electrically conductive colloidal systems is left for further study.

Conclusions

The electronic transport timescale in sheared carbon black suspensions was determined from the ac conductivity extracted from rheo-electric measurements of Vulcan XC72R carbon black suspended in Newtonian fluids spanning a broad range of viscosity and polarity. Comparisons of the macroscopic properties of these suspensions in the quiescent state as a function of carbon black loading revealed an increase in elasticity correlated to an increase in conductivity, consistent with prior literature. However, gels prepared in solvents of different polarity with the same elastic modulus exhibited conductivity that depended sensitively on the solvent polarity and dielectric constant, implicating the important role of the suspending fluid in mediating electrical transport between and within carbon black agglomerates. In the strong flow regime, the electrical behavior of all suspensions were compared on an equivalent microstructural basis using the agglomerate volume fraction, calculated from the relative viscosity measured for each suspension. This structure-conductivity relationship could not be rationalized by existing tunneling-based models used to predict the conductivity in polymer composites even when accounting for changing agglomerate size on the conductivity.

Instead, accounting for shear-induced particle dynamics on the electron transport timescale (recently developed to describe the electron transport rate in non-Brownian suspensions) showed empirical collapse across all suspensions tested with the fluid Mason number. As the fluid Mason number represents an equivalent microstructural basis at a given carbon black volume fraction, this collapse confirmed that the transport timescale is strongly influenced by the shear induced dynamics in the strong flow regime. As the conductivity is directly influenced by the transport timescale, these findings show that dynamics are a critical contribution to the conduction process in flowing suspensions of carbon black. Finally, the strong dependence of the conductivity on the polarity of the solvent motivates future work to developed quantitative models that incoporate the suspending fluid dielectric properties.

Materials and Methods

The high-structured carbon black studied was Vulcan XC72R from Cabot Corporation (Boston, MA, USA). Hexadecane (HD) and light mineral oil (MO) were bought from MilliporeSigma (St. Louis, MO, USA). Propylene carbonate (PC) and ethylene glycol (EG) were obtained from Thermo Fisher Scientific (Waltham, MA, USA). These four solvents were selected for their wide span of dielectric strength (ε_f), viscosities (η_f), and densities (ρ) as outlined in **Table S1**. Preparation of the carbon black suspensions followed previously established procedures that utilized high shear intensities to break down and fully disperse the carbon black primary aggregates (11, 34). Carbon black was dispersed in each of the four solvents at three different weight fractions (w) based on their dry mass. The range of w lies above the mechanical and electrical percolation threshold and were chosen such that the dry carbon black volume fraction (ϕ_{dry}) is identical across all solvents. w was converted to ϕ_{dry} using a dry mass density of 1.8 g/mL for Vulcan XC72R. Furthermore, ϕ_{dry} was rescaled to the shear-independent effective carbon black volume fraction (ϕ_{eff}) with the porosity of the primary particle and aggregate ($\Phi_{p,agg}$) following $\phi_{eff} = \phi_{dry}/\Phi_{p,agg}$. $\Phi_{p,agg}$ was found to be 0.2 in previous literature through small-angle neutron scattering experiments (19).

Rheological measurements were taken on a TA Instruments ARES G2 strain-controlled rheometer equipped with a custom-built Couette geometry (titanium, ID = 26 mm, OD = 27 mm, base gap = 0.5 mm, see Fig S9) maintained at a temperature of 25°C using a forced convection oven connected to a liquid nitrogen source. Mechanical percolation of the carbon black microstructure was confirmed through small amplitude oscillatory shear measurements with a 0.1% strain amplitude over a frequency of 10 to 0.1 rad/s. Flow curves were constructed using an established protocol that allows for the inspection of sedimentation in the suspensions (33, 34). Shortly after loading, samples were presheared at a shear rate of 2500 s⁻¹ until a steady-state stress was achieved (at least 10 min). Then, constant shear was applied to the suspensions in a descending stepwise fashion from 2500 to 10 s⁻¹ for at least 3 min at each shear rate of interest. A 0 s⁻¹ resting period was applied after each shear step, followed by a short preshear to erase any mechanical history before the next shear step.

The shear-dependent dielectric properties were measured simultaneously with the steady shear rheology experiments. For the propylene carbonate suspensions, the dielectric response was probed using an Agilent 4980A LCR meter at the NIST Center for Neutron Research over a frequency range (f) of 20 Hz to 2 MHz (52, 53). For all other suspensions, the dielectric response was probed using a Keysight E4990A Impedance Analyzer at Northwestern University over a frequency range of 20 Hz to 50 MHz. In all cases, the sample impedance was taken across the shear gap of the Couette as described in Fig S9, in the direction of the shear gradient (1-2 plane), at a temperature of 25°C. The raw data was corrected for the residual impedance of the short circuit and stray admittance of the open circuit using standard reductions (52). The complex permittivity (ε^*) and conductivity (κ) were calculated from the corrected complex impedance (Z^*) following $\varepsilon^* = C/Z^*i\omega\varepsilon_0$ and $\kappa = Re(C/Z^*)$ where C is the Couette cell constant, i is the imaginary unit, ε_0 is the vacuum permittivity, and ω is the angular frequency given as $\omega = 2\pi f$, with Re signifying the real component of a complex number.

Acknowledgments

P.Z.R. was funded by the National Science Foundation under Grant No. CBET-2047365 and DMR-1720139-006. Q.L. was funded by the U.S. Department of Energy, Office of Science, Office of Basic Energy Sciences under Award No. DE-SC-0022119. Q.L. gratefully acknowledges support from the Ryan Fellowship and the International Institute for Nanotechnology at Northwestern University. N.J.W., J.J.R., and J.B.H. were funded by a cooperative agreement with the NIST Center for Neutron Research #70NANB17H302.

References

- 1. K. B. Hatzell, M. Boota, Y. Gogotsi, Materials for suspension (semi-solid) electrodes for energy and water technologies. *Chem Soc Rev* **44**, 8664–8687 (2015).
- 2. M. Duduta, et al., Semi-solid lithium rechargeable flow battery. Adv Energy Mater 1, 511–516 (2011).
- 3. J. J. Warren, M. E. Ener, A. Vlček, J. R. Winkler, H. B. Gray, Electron hopping through proteins. *Coord Chem Rev* **256**, 2478–2487 (2012).
- 4. P. Z. Ramos, A. Sarmah, M. J. Green, J. J. Richards, In situ investigation of the rheological and dielectric properties of a cross-linking carbon nanotube-thermosetting epoxy. *Soft Matter* **19**, 6168–6175 (2023).
- 5. W. Zhang, P. Feng, J. Chen, Z. Sun, B. Zhao, Electrically conductive hydrogels for flexible energy storage systems. *Prog Polym Sci* **88**, 220–240 (2019).
- 6. M. Jalali, S. Dauterstedt, A. Michaud, R. Wuthrich, Electromagnetic shielding of polymer—matrix composites with metallic nanoparticles. *Compos B Eng* **42**, 1420–1426 (2011).
- 7. M. Amjadi, A. Pichitpajongkit, S. Lee, S. Ryu, I. Park, Highly stretchable and sensitive strain sensor based on silver nanowire-elastomer nanocomposite. *ACS Nano* **8**, 5154–5163 (2014).
- 8. G. Spinelli, *et al.*, Rheological and electrical behaviour of nanocarbon/poly(lactic) acid for 3D printing applications. *Compos B Eng* **167**, 467–476 (2019).
- 9. H. Jun Park, *et al.*, Fluid-Dynamics-Processed Highly Stretchable, Conductive, and Printable Graphene Inks for Real-Time Monitoring Sweat during Stretching Exercise. *Adv Funct Mater* **31**, 2011059 (2021).
- 10. R. M. Saraka, S. L. Morelly, M. H. Tang, N. J. Alvarez, Correlating Processing Conditions to Short- And Long-Range Order in Coating and Drying Lithium-Ion Batteries. *ACS Appl Energy Mater* **3**, 11681–11689 (2020).
- 11. P. Z. Ramos, C. C. Call, L. V. Simitz, J. J. Richards, Evaluating the Rheo-electric Performance of Aqueous Suspensions of Oxidized Carbon Black. *J Colloid Interface Sci* **634**, 379–387 (2023).
- 12. K. B. Hatzell, *et al.*, Effect of oxidation of carbon material on suspension electrodes for flow electrode capacitive deionization. *Environ Sci Technol* **49**, 3040–3047 (2015).
- 13. G. Ambrosetti, *et al.*, Solution of the tunneling-percolation problem in the nanocomposite regime. *Phys Rev B Condens Matter Mater Phys* **81**, 1–12 (2010).
- 14. K. M. Jäger, D. H. McQueen, I. A. Tchmutin, N. G. Ryvkina, M. Klüppel, Electron transport and ac electrical properties of carbon black polymer composites. *J Phys D Appl Phys* **34**, 2699 (2001).
- 15. Q. Liu, J. J. Richards, Rheo-electric measurements of carbon black suspensions containing polyvinylidene difluoride in N-methyl-2-pyrrolidone. *J Rheol (N Y N Y)* **67**, 647–659 (2023).
- 16. D. Strugova, É. David, N. R. Demarquette, Effect of steady shear deformation on electrically conductive PP/PS/MWCNT composites. *J Rheol (N Y N Y)* **67**, 977–993 (2023).
- 17. H. Yu, K. D. Potter, M. R. Wisnom, A novel manufacturing method for aligned discontinuous fibre composites (High Performance-Discontinuous Fibre method). *Compos Part A Appl Sci Manuf* **65**, 175–185 (2014).
- 18. H. Lin, *et al.*, Quantifying the hydrodynamic contribution to electrical transport in non-Brownian suspensions. *Proc Natl Acad Sci U S A* **119**, e2203470119 (2022).
- 19. J. J. Richards, J. B. Hipp, J. K. Riley, N. J. Wagner, P. D. Butler, Clustering and Percolation in Suspensions of Carbon Black. *Langmuir* **33**, 12260–12266 (2017).
- 20. J. Mewis, N. J. Wagner, Colloidal suspension rheology. *Colloidal Suspension Rheology* **9780521515**, 1–393 (2011).
- 21. E. S. P. B. V, J. Mewis, L. M. De Groot, J. A. Helsen, Dielectric behaviour of flowing thixotropic suspensions. *Colloids and Surfaces* **22**, 249–269 (1987).
- 22. U. Genz, J. A. Helsen, J. Mewis, Dielectric spectroscopy of reversibly flocculated dispersions during flow. *J Colloid Interface Sci* [Preprint] (1994).
- 23. M. Youssry, *et al.*, Non-aqueous carbon black suspensions for lithium-based redox flow batteries: Rheology and simultaneous rheo-electrical behavior. *Physical Chemistry Chemical Physics* **15**, 14476–14486 (2013).

- 24. M. Meslam, A. A. Elzatahry, M. Youssry, Promising aqueous dispersions of carbon black for semisolid flow battery application. *Colloids Surf A Physicochem Eng Asp* **648** (2022).
- 25. A. Helal, T. Divoux, G. H. McKinley, Simultaneous Rheoelectric Measurements of Strongly Conductive Complex Fluids. *Phys Rev Appl* **6**, 1–19 (2016).
- 26. I. Balberg, Tunnelling and percolation in lattices and the continuum. *J Phys D Appl Phys* **42** (2009).
- 27. H. A. Barnes, Thixotropy—a review. J Nonnewton Fluid Mech 70, 1–33 (1997).
- 28. G. Ovarlez, L. Tocquer, F. Bertrand, P. Coussot, Rheopexy and tunable yield stress of carbon black suspensions. *Soft Matter* **9**, 5540–5549 (2013).
- 29. Y. Wang, R. H. Ewoldt, New insights on carbon black suspension rheology—Anisotropic thixotropy and antithixotropy. *J Rheol (N Y N Y)* **66**, 937–953 (2022).
- 30. K. Dullaert, J. Mewis, Stress jumps on weakly flocculated dispersions: Steady state and transient results. *J Colloid Interface Sci* **287**, 542–551 (2005).
- 31. C. O. Osuji, D. A. Weitz, Highly anisotropic vorticity aligned structures in a shear thickening attractive colloidal system. *Soft Matter* **4**, 1388–1392 (2008).
- 32. C. O. Osuji, C. Kim, D. A. Weitz, Shear thickening and scaling of the elastic modulus in a fractal colloidal system with attractive interactions. *Phys Rev E Stat Nonlin Soft Matter Phys* **77**, 8–11 (2008).
- 33. J. B. Hipp, J. J. Richards, N. J. Wagner, Structure-property relationships of sheared carbon black suspensions determined by simultaneous rheological and neutron scattering measurements. *J Rheol (N Y N Y)* **63**, 423–436 (2019).
- 34. J. B. Hipp, J. J. Richards, N. J. Wagner, Direct measurements of the microstructural origin of shear-thinning in carbon black suspensions. *J Rheol (N Y N Y)* **65**, 145–157 (2021).
- 35. A. Narayanan, F. Mugele, M. H. G. Duits, Mechanical History Dependence in Carbon Black Suspensions for Flow Batteries: A Rheo-Impedance Study. *Langmuir* **33**, 1629–1638 (2017).
- 36. T. Amari, K. Watanabe, Flow properties and electrical conductivity of carbon black—linseed oil suspension. *J Rheol (N Y N Y)* **34**, 207–221 (1990).
- 37. W. H. Herschel, R. Bulkley, Konsistenzmessungen von Gummi-Benzollösungen. *Kolloid-Zeitschrift* **39**, 291–300 (1926).
- 38. A. Z. Nelson, R. H. Ewoldt, Design of yield-stress fluids: a rheology-to-structure inverse problem. *Soft Matter* **13**, 7578–7594 (2017).
- 39. Z. Varga, J. W. Swan, Large scale anisotropies in sheared colloidal gels. *J Rheol (N Y N Y)* **62**, 405–418 (2018).
- 40. I. M. Krieger, T. J. Dougherty, A Mechanism for Non-Newtonian Flow in Suspensions of Rigid Spheres. *Transactions of The Society of Rheology* **3**, 137–152 (1959).
- 41. T. Wang, M. J. Ni, Z. Y. Luo, C. H. Shou, K. F. Cen, Viscosity and aggregation structure of nanocolloidal dispersions. *Chinese Science Bulletin* **57**, 3644–3651 (2012).
- 42. F. Kremer, A. Schonhals, Eds., *Broadband Dielectric Spectroscopy*, 1st Ed. (Springer Berlin Heidelberg, 2003).
- 43. J. Gavis, Transport of electric charge in low dielectric constant fluids. *Chem Eng Sci* **19**, 237–252 (1964).
- 44. N. Prokopuk, K. A. Son, C. Waltz, Electron tunneling through fluid solvents. *Journal of Physical Chemistry C* **111**, 6533–6537 (2007).
- 45. H. B. Gray, J. R. Winkler, Long-range electron transfer. *Proc Natl Acad Sci U S A* **102**, 3534–3539 (2005).
- R. Pelster, U. Simon, Nanodispersions of conducting particles: Preparation, microstructure and dielectric properties. *Colloid Polym Sci* 277, 2–14 (1999).
- 47. V. Trappe, D. A. Weitz, Scaling of the viscoelasticity of weakly attractive particles. *Phys Rev Lett* **85** (2000).
- 48. D. Untereker, S. Lyu, J. Schley, G. Martinez, L. Lohstreter, Maximum conductivity of packed nanoparticles and their polymer composites. *ACS Appl Mater Interfaces* **1**, 97–101 (2009).
- 49. I. Balberg, S. A. Sunshine, M. B. Heaney, Critical behavior of the electrical transport properties in a tunneling-percolation system. *Phys Rev B* **59**, 12196 (1999).

- 50. N. F. Carnahan, K. E. Starling, Equation of State for Nonattracting Rigid Spheres. *J Chem Phys* **51**, 635–636 (1969).
- 51. A. M. Leshansky, J. F. Morris, J. F. Brady, Collective diffusion in sheared colloidal suspensions. *J Fluid Mech* **597**, 305–341 (2008).
- 52. J. J. Richards, N. J. Wagner, P. D. Butler, A strain-controlled RheoSANS instrument for the measurement of the microstructural, electrical, and mechanical properties of soft materials. *Review of Scientific Instruments* **88** (2017).
 - 53. J. J. Richards, C. V. L. Gagnon, J. R. Krzywon, N. J. Wagner, P. D. Butler, Dielectric RheoSANS Simultaneous interrogation of impedance, rheology and small angle neutron scattering of complex fluids. *Journal of Visualized Experiments* **2017**, 1–11 (2017).

Figures and Tables

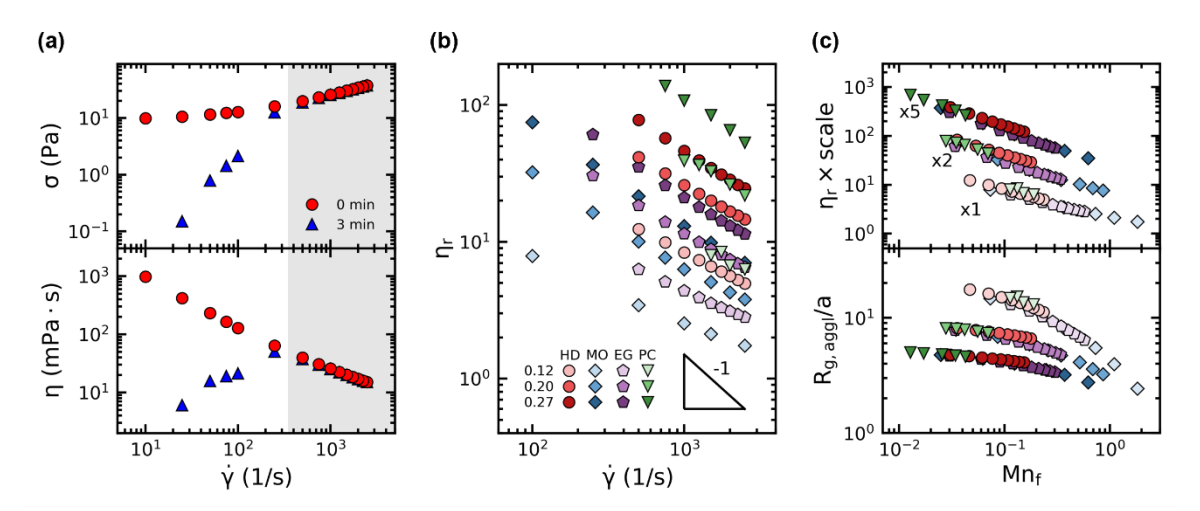


Figure 1. (a) The shear stress, σ , and viscosity, η , of ϕ_{eff} = 0.12 carbon black suspended in hexadecane at various shear rates, $\dot{\gamma}$. The time dependency of the measured response is compared at 0 and 3 minutes. The shaded region highlights the regime of strong flow. (b) The relative viscosity, η_r , of all formulated carbon black suspensions for shear rates that fall within their respective strong flow regimes. (c) η_r and the relative agglomerate size, $R_{g,aggl}/\alpha$, as a function of the fluid Mason number, Mn_f , for all formulated carbon black suspensions. η_r is scaled for each given set of ϕ_{eff} to better visualize the collapse of the data.

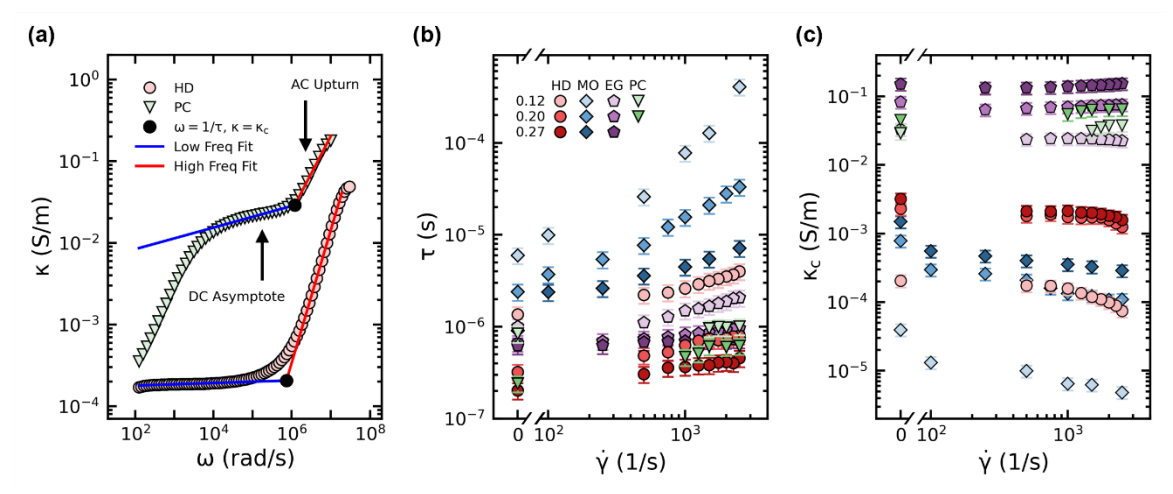


Figure 2. (a) An example of the conductivity spectra and model-independent fits on ϕ_{eff} = 0.12 CB in hexadecane, HD, and propylene carbonate, PC, in the quiescent state. Two power laws converge at a given frequency that defines the electron transport time, τ , and characteristic conductivity, κ_c , of the CB electron carriers. (b-c) τ and κ_c plotted against the applied shear rate, $\dot{\gamma}$, for the given suspensions. Error bars represent a 20% departure from the measured values. The x-axis includes $\dot{\gamma}$ = 0 s⁻¹ and is scaled logarithmically for $\dot{\gamma}$ ≥ 100 s⁻¹.

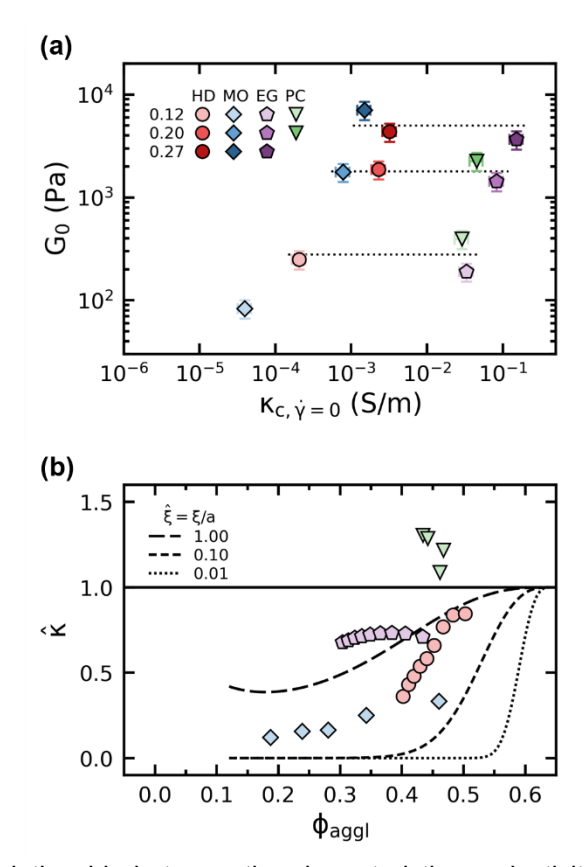


Figure 3. (a) Scaling relationship between the characteristic conductivity at the quiescent state, $\kappa_{c,\dot{\gamma}=0}$, and the plateau modulus, G_0 , for all formulated CB suspensions. Error bars represent a 20% departure from the measured values. The horizontal, dotted lines are meant to guide the eyes when comparing data at fixed effective volume fraction, ϕ_{eff} . (b) The relative conductivity, $\hat{\kappa}=\kappa_c/\kappa_{c,\dot{\gamma}=0}$ for $\phi_{eff}=0.12$ CB suspensions versus their estimated agglomerate volume fraction, ϕ_{aggl} . The horizontal, solid line demarks a $\kappa_c/\kappa_{c,\dot{\gamma}=0}$ value of 1. The dashed curves demark the predicted normalized conductivity based on the critical path framework described in the main text for several dimensionless hopping distances, $\hat{\xi}$. The conductivity predictions are truncated at $\phi_{aggl}=0.12$ as ϕ_{aggl} cannot fall below ϕ_{eff} .

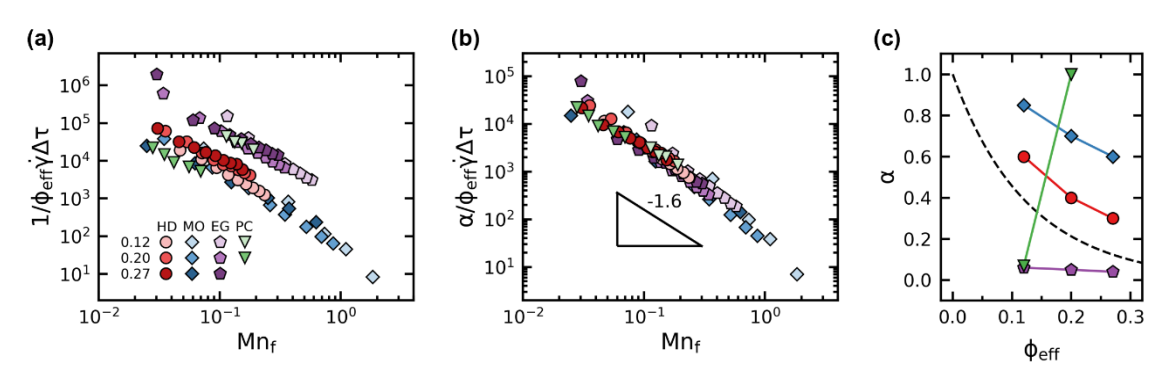


Figure 4. (a) $g(\phi) = 1/\phi_{eff}\dot{\gamma}\Delta\tau$ versus the fluid Mason number, Mn_f , for each formulated suspension. The physical representation of $g(\phi)$ is described in the main text. (b) $g(\phi)$ rescaled to an empirical parameter, α , once more plotted against Mn_f . A fit to the data reveals a power law scaling of -1.6. (c) α as a function of the effective volume fraction, ϕ_{eff} , for each formulated suspension. The solid lines between subsequent points for a given suspending fluid are meant to guide the eyes. The black, dashed curve is the Carnahan-Starling expression that represents the zero wave-vector limit of the hard spheres structure factor.



Supporting Information for

Quantifying electron transport in aggregated colloidal suspensions in the strong slow regime

Julie B. Hipp^{b,c,1}, Paolo Z. Ramos^{a,1}, Qingsong Liu^a, Norman J. Wagner^b, Jeffrey J. Richards^{a,*}

- ^a Department of Chemical and Biological Engineering, Northwestern University, Evanston, IL 60208, USA
- ^b Center for Neutron Science, Department of Chemical and Biomolecular Engineering, University of Delaware, Newark, DE 19716, USA
- ^c Current affiliation: Julie B. Hipp, The Procter & Gamble Company, Cincinnati, OH 45202, USA
- * Corresponding author: Jeffrey J. Richards

Email: jeffrey.richards@northwestern.edu

This PDF file includes:

Supporting Text Table S1 Figures S1 to S8 SI References

Supporting Information Text

<u>Time-dependent stress and viscosity response:</u>

The stress, σ , and viscosity, η , measured at 0 and 3 minutes against the applied shear rate, $\dot{\gamma}$, for each suspension are shown in **Figure S1**. The strong flow regime encompasses shear rates above a critical shear rate where the rheological response does not vary significantly with time (25, 28, 31, 33). In these conditions, CB agglomerates undergo self-similar structural change by decreasing in size with increasing shear intensity while maintaining a constant fractal dimension (33, 34). This results in a steady increase in σ with shear rate is observed accompanied by a shear-thinning response in η due to the breakdown of the agglomerates (30). Below the critical shear condition, various heterogeneities in the suspensions emerge due to the densification and sedimentation of the carbon black agglomerates. This leads to a drop in σ over time and an apparent shear-thickening behavior in η , with lower shear rates enhancing this rheopectic response. This stark transition marked by a critical shear rate is often called a stress-response bifurcation and has been observed frequently in prior literature (28, 32, 33).

Herschel-Bulkley fits of the flow curves:

The instantaneous, 0 min response in the stress, $\sigma_{t=0}$, at each shear rate is plotted in **Figure S2**. Each flow curve was fit to the Herschel-Bulkley model given as $\sigma_{t=0} = \sigma_y (1 + (\dot{\gamma}/\dot{\gamma}_c)^n)$ to obtain the Herschel-Bulkley yield stress, σ_y , critical shear rate, $\dot{\gamma}_c$, and the power law index, $\dot{\gamma}_c$, as shown on the subplots. The fits were performed such that the X^2 values are minimized. The use of the instantaneous flow curve to fit the model above follows previously established work on carbon black suspensions (34). Comparison of the obtained parameters with that from previous work shows good agreement. Note that $\dot{\gamma}_c$ represents that shear rate corresponding to a shear stress that is twice the value of σ_y and should not be confused with the critical shear condition that designates the weak and strong flow regime.

Analysis of the frequency-dependent dielectric permittivity:

The frequency-dependent dielectric response of the neat solvents in the quiescent state taken at 25°C is presented in **Figure S3**. HD and MO are nonpolar, non-ionogenic fluids and did not exhibit a relaxation process along the real component of the permittivity, ε' , in the frequency domain, ω probed. The absence of dipolar fluctuations makes the solvents electrically insulating with non-observable conductivities, κ . On the other hand, PC and EG are polar fluids with high dielectric strengths and values of ε' orders of magnitude greater. In the presence of an electric field, charge separation occurs in that a layer of counterions form along the walls of the Couette geometry. This electrode polarization effect can be discerned as the steep decrease in ε' at low frequencies (42). Furthermore, migration of charges leads to ionic conduction through the fluid of about 2 x 10⁻⁴ S/m that is frequency independent.

The addition of 12 vol% carbon black to the solvents further augments the dielectric response. The conductivities for the filled suspensions far exceed those of the neat fluids across all frequencies and for all suspensions. Under an oscillating electric field, the carbon black agglomerates polarize, and ε' rises significantly across the entire frequency domain. The low frequency relaxation in ε' from electrode polarization for carbon black in PC and EG is also heightened. This stems from additional double layers that form on the solid-liquid interface between the particles and the solvent (11). The Debye relaxation process is observed with the onset of a stepwise decrease in ε' with increasing frequency. Before this decrease is a plateau that in essence represents the static permittivity, ε_s . It is in this location where we extracted ε_s at a given frequency for each suspension for the calculation seen in **Figure S5**.

Table S1. Mechanical and dielectric properties of the suspending fluids used to formulate carbon black suspensions of specified carbon content.

Suspending Fluid	Туре	$arepsilon_f$	η_f (mPa·s)	ρ_f (g/cm ³)	w×100%	φ _{eff} ×100%
Hexadecane (HD)	Nonpolar	2.1	3.03	0.77	5.4, 8.8, 11.7	12, 20, 27
Light Mineral Oil (MO)	Nonpolar	2.4	26.0	0.84	5.0, 8.2, 11.0	12, 20, 27
Ethylene Glycol (EG)	Polar Protic	37	18.4	1.11	3.8, 6.3, 8.5	12, 20, 27
Propylene Carbonate (PC)	Polar Aprotic	64	2.50	1.20	3.6, 5.9, 7.9	12, 20, 27

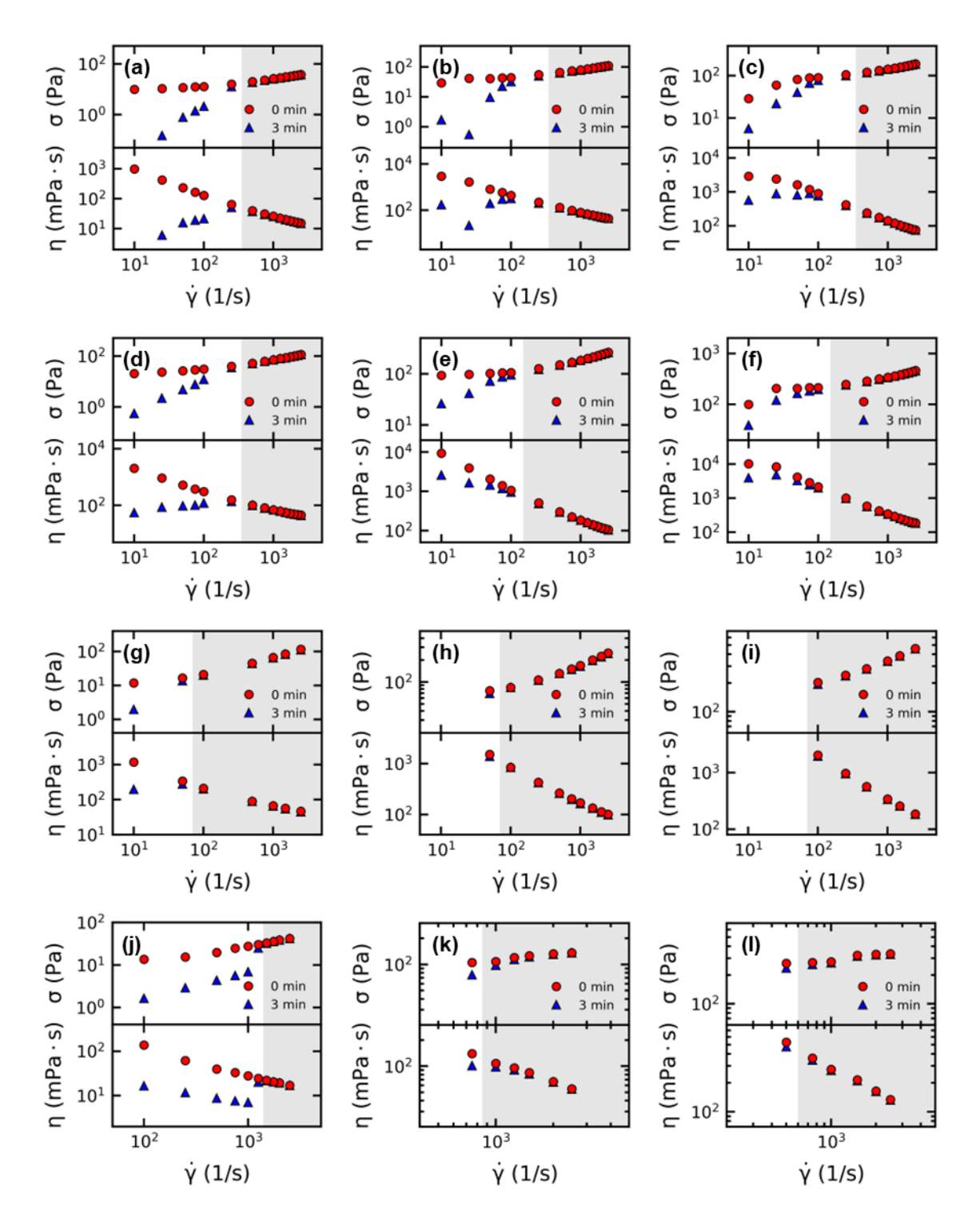


Fig. S1. The shear stress, σ , and viscosity, η , of carbon black suspensions in hexadecane [ϕ_{eff} = (a) 0.12, (b) 0.20, (c) 0.27], ethylene glycol [ϕ_{eff} = (d) 0.12, (e) 0.20, (f) 0.27], mineral oil [ϕ_{eff} = (g) 0.12, (h) 0.20, (i) 0.27], and propylene carbonate [ϕ_{eff} = (j) 0.12, (k) 0.20, (l) 0.27] at various shear rates, $\dot{\gamma}$. The time dependency of the measured response is compared at 0 and 3 minutes. The shaded region highlights shear rates that fall into the regime of strong flow.

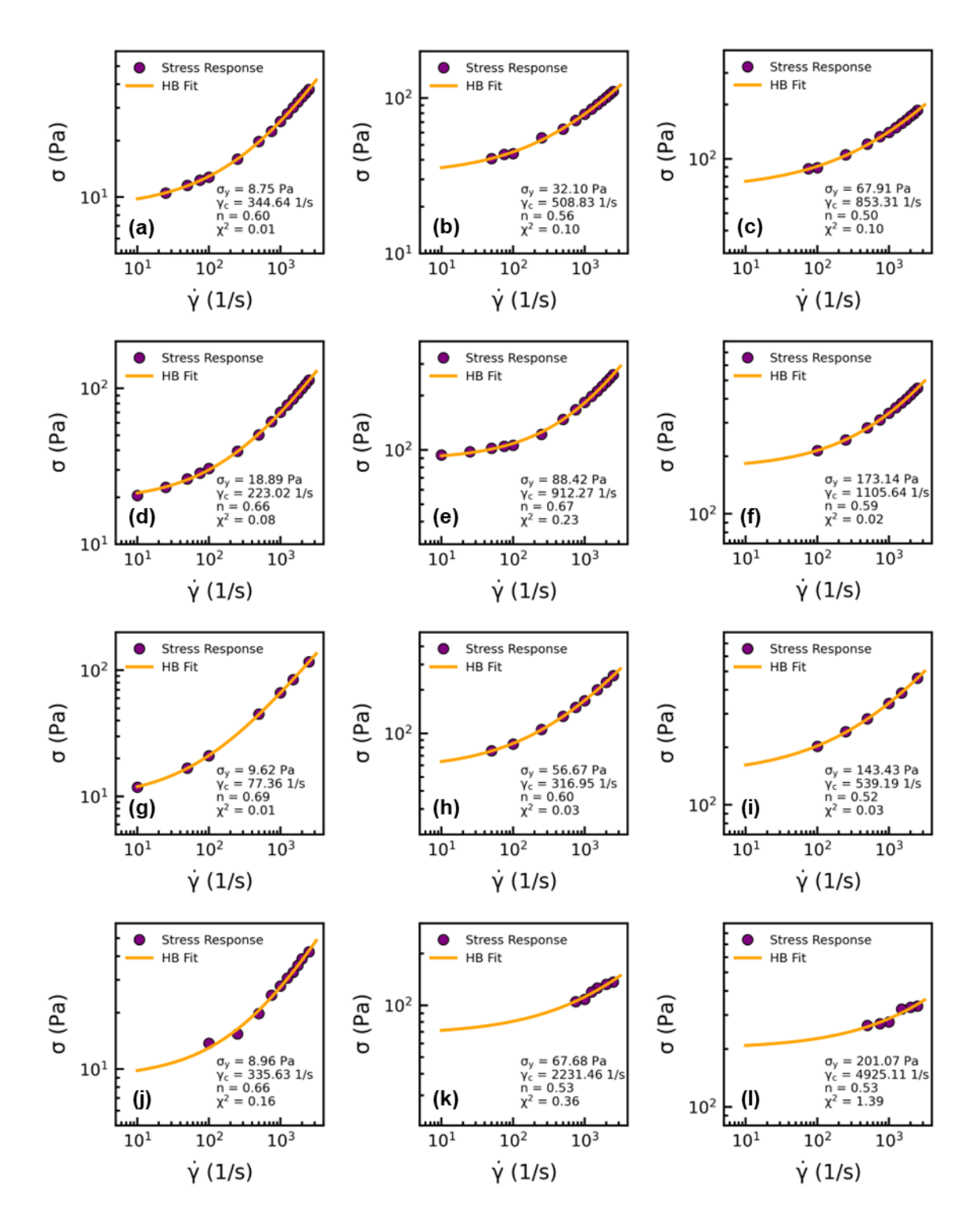


Fig. S2. The shear stress, σ , of carbon black suspensions in hexadecane [ϕ_{eff} = (a) 0.12, (b) 0.20, (c) 0.27], ethylene glycol [ϕ_{eff} = (d) 0.12, (e) 0.20, (f) 0.27], mineral oil [ϕ_{eff} = (g) 0.12, (h) 0.20, (i) 0.27], and propylene carbonate [ϕ_{eff} = (j) 0.12, (k) 0.20, (l) 0.27] at various shear rates, $\dot{\gamma}$. The solid, yellow curve fits the stress response to the Herschel Bulkley equation, with parameters shown on each subplot.

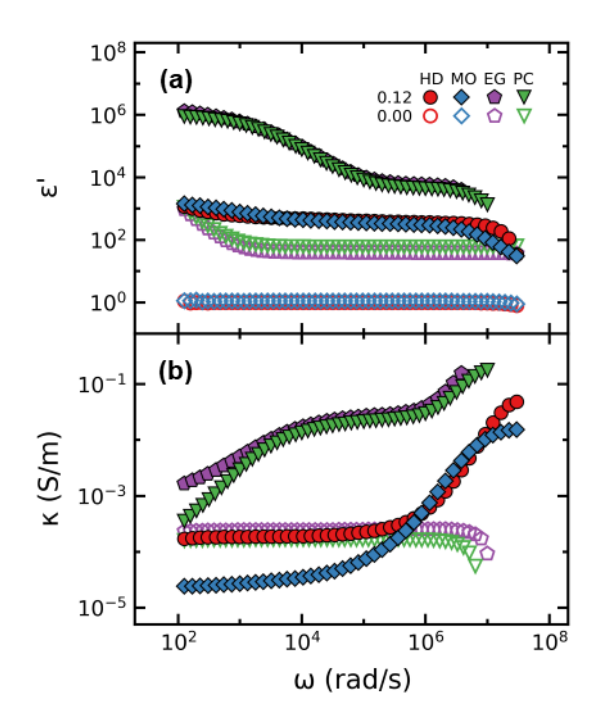


Fig. S3. Frequency sweep, ω , of (a) the real component of the permittivity, ε' , and (b) the conductivity, κ , of $\phi_{eff}=0.12$ CB suspensions (filled markers) and $\phi_{eff}=0.00$ neat solvents (hollow markers) in the absence of shear flow. The conductivity of neat MO and HD is non-observable in (b) due to the electrically-insulative nature of the fluids.

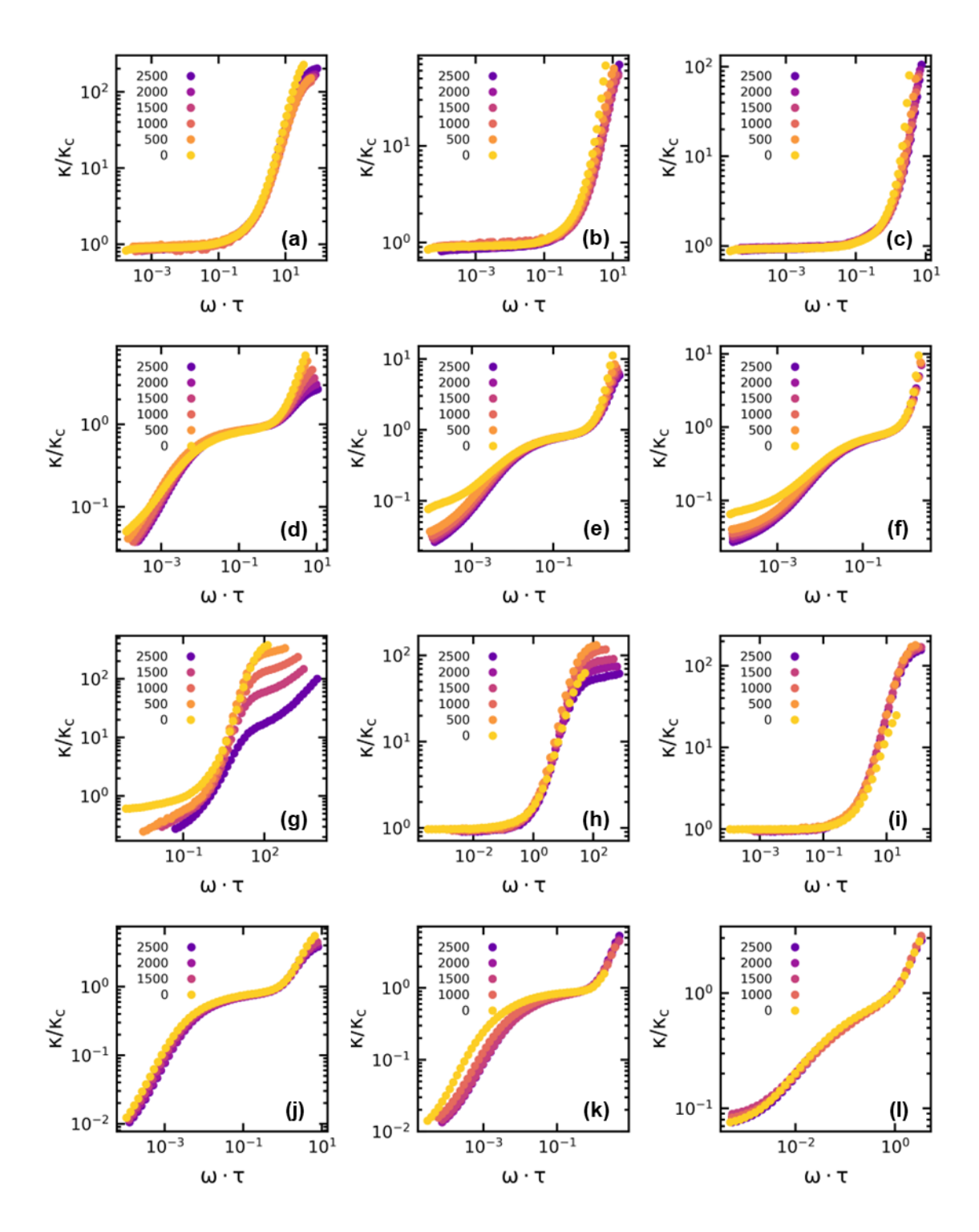


Fig. S4. Master curves of the shear rate-dependent normalized conductivity, κ/κ_c , versus the normalized frequency, $\omega \cdot \tau$, for carbon black suspensions in hexadecane [ϕ_{eff} = (a) 0.12, (b) 0.20, (c) 0.27], ethylene glycol [ϕ_{eff} = (d) 0.12, (e) 0.20, (f) 0.27], mineral oil [ϕ_{eff} = (g) 0.12, (h) 0.20, (i) 0.27], and propylene carbonate [ϕ_{eff} = (j) 0.12, (k) 0.20, (l) 0.27]. Not all shear rates tested are shown. Selected shear rates are given by the legend of each subplot. The process of acquiring κ_c and τ is described in the main text.

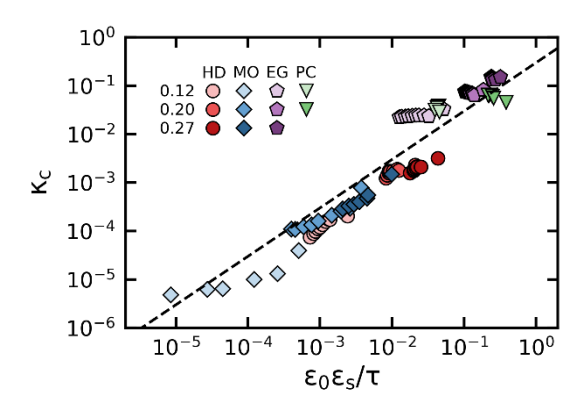


Fig. S5. The characteristic conductivity, κ_c , versus $\varepsilon_0 \varepsilon_s / \tau$ where ε_0 is the permittivity of free space, ε_s is the static permittivity, and τ is the charge transport time. The dashed, black line shows a $\kappa_c = p\varepsilon_0 \varepsilon_s / \tau$ relation with p representing a phenomenological constant, here plotted as 0.3. Acquiring κ_c and τ is described in the main text. The processing of acquiring ε_s is described in the supporting information text.

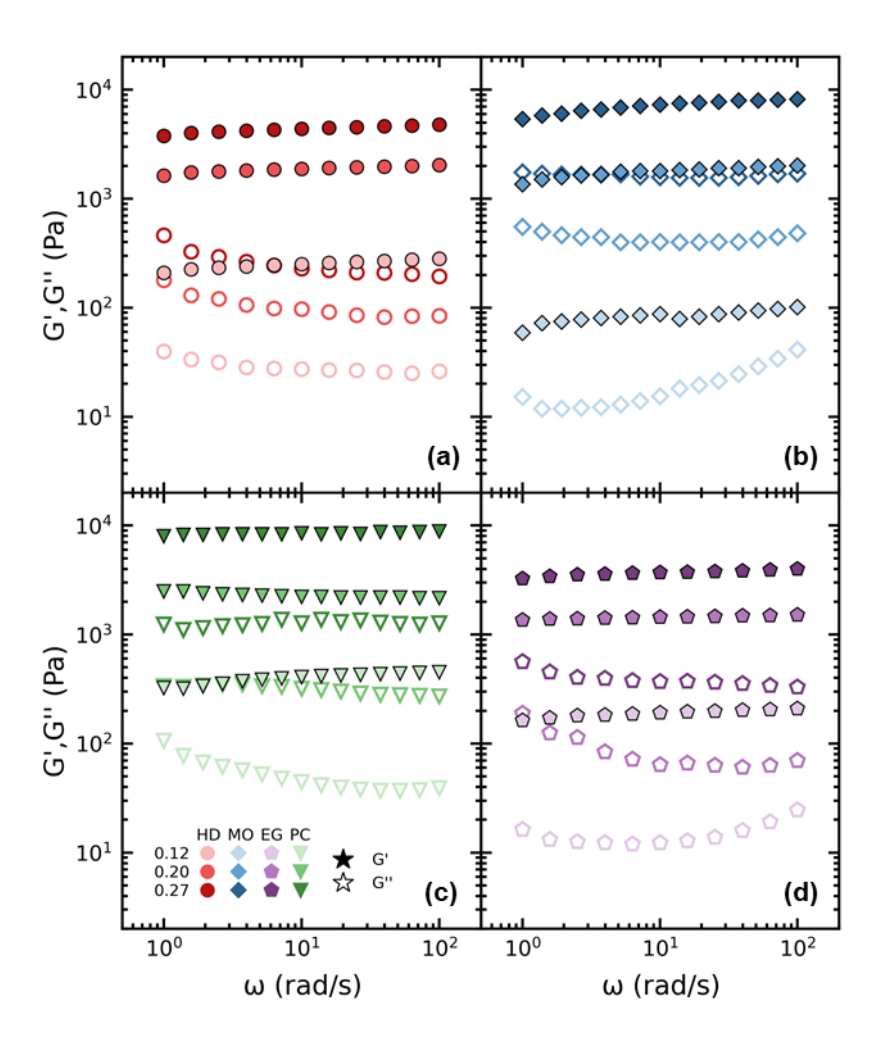


Fig. S6. Small amplitude oscillatory shear measurements of the storage, G', and loss, G'', modulus in the frequency range, ω , of 1 to 100 rad/s for ϕ_{eff} = 0.12, 0.20, 0.27 CB suspensions in (a) hexadecane, (b) mineral oil, (c) propylene carbonate, and (d) ethylene glycol. Filled and hollow markers denote G' and G'', respectively, as indicated in the legend.

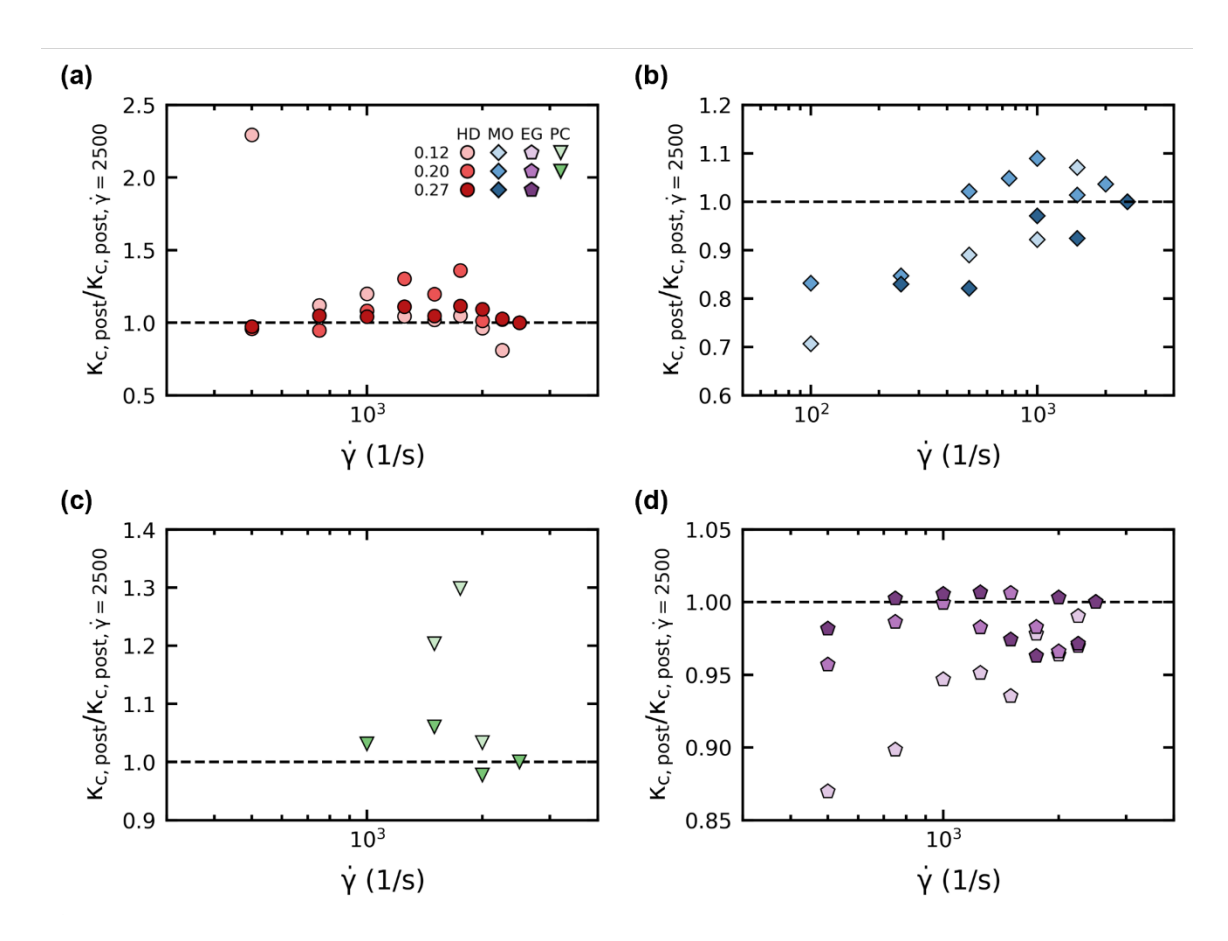


Fig. S7. The applied shear rate, $\dot{\gamma}$, versus the post shear step quiescent conductivity, $\kappa_{c,post}$, relative to the post shear step quiescent conductivity at $\dot{\gamma}$ = 2500 1/s for ϕ_{eff} = 0.12, 0.20, 0.27 CB suspensions in (a) hexadecane, (b) mineral oil, (c) propylene carbonate, and (d) ethylene glycol.

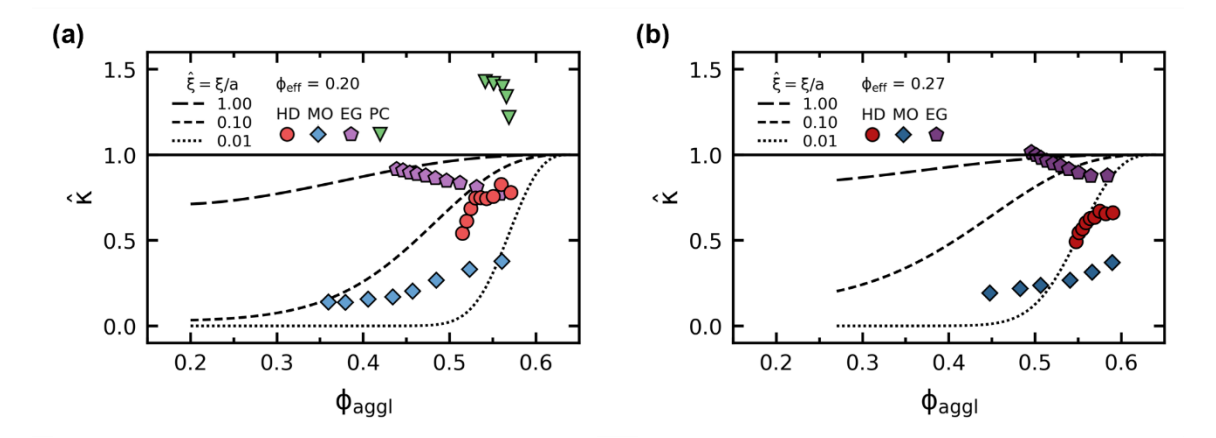


Fig. S8. The relative conductivity, $\hat{\kappa}$, for (a) $\phi_{eff} = 0.20$ and (b) $\phi_{eff} = 0.27$ CB suspensions versus the agglomerate volume fraction, ϕ_{aggl} . The horizontal, solid line demarks a $\hat{\kappa}$ value of 1. The dashed curves demark the predicted relative conductivity based on the critical path framework for several dimensionless hopping distances, $\hat{\xi}$. The process of acquiring $\hat{\kappa}$, ϕ_{aggl} , and the critical path prediction is described in the main text.

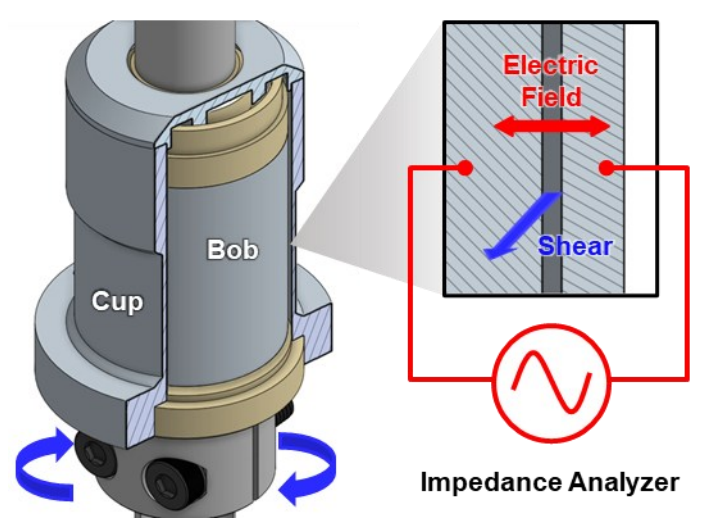


Fig. S9. CAD section view of the custom-built dielectric Couette geometry for the ARES-G2 rheometer. The cup rotates or oscillates to apply a strain on the sample, while the bob remains stationary and measures the resulting torque. The walls of the cup and bob are electrically connected to an impedance analyzer. The impedance of the sample is measured simultaneously as the sample is deformed.

SI References

- 1. C. O. Osuji, D. A. Weitz, Highly anisotropic vorticity aligned structures in a shear thickening attractive colloidal system. *Soft Matter* **4**, 1388–1392 (2008).
- 2. G. Ovarlez, L. Tocquer, F. Bertrand, P. Coussot, Rheopexy and tunable yield stress of carbon black suspensions. *Soft Matter* **9**, 5540–5549 (2013).
- 3. J. B. Hipp, J. J. Richards, N. J. Wagner, Structure-property relationships of sheared carbon black suspensions determined by simultaneous rheological and neutron scattering measurements. *J Rheol (N Y N Y)* **63**, 423–436 (2019).
- 4. A. Helal, T. Divoux, G. H. McKinley, Simultaneous Rheoelectric Measurements of Strongly Conductive Complex Fluids. *Phys Rev Appl* **6**, 1–19 (2016).
- 5. J. B. Hipp, J. J. Richards, N. J. Wagner, Direct measurements of the microstructural origin of shear-thinning in carbon black suspensions. *J Rheol (N Y N Y)* **65**, 145–157 (2021).
- 6. K. Dullaert, J. Mewis, Stress jumps on weakly flocculated dispersions: Steady state and transient results. *J Colloid Interface Sci* **287**, 542–551 (2005).
- 7. C. O. Osuji, C. Kim, D. A. Weitz, Shear thickening and scaling of the elastic modulus in a fractal colloidal system with attractive interactions. *Phys Rev E Stat Nonlin Soft Matter Phys* **77**, 8–11 (2008).
- 8. F. Kremer, A. Schonhals, Eds., *Broadband Dielectric Spectroscopy*, 1st Ed. (Springer Berlin Heidelberg, 2003) https://doi.org/10.1007/978-3-642-56120-7.
- 9. P. Z. Ramos, C. C. Call, L. V. Simitz, J. J. Richards, Evaluating the Rheo-electric Performance of Aqueous Suspensions of Oxidized Carbon Black. *J Colloid Interface Sci* **634**, 379–387 (2023).